

# Perturbation expansion for 2-D Hubbard model

V. Zlatić, B. Horvatić and B. Dolički

*Institute of Physics, Bijenička cesta 46, P. O. Box 304,  
HR-10001 Zagreb, Croatia*

S. Grabowski and P. Entel

*Gerhard-Mercator University, D-47048 Duisburg, Germany*

K.-D. Schotte

*Institut für Theoretische Physik, Freie Universität Berlin,  
Arnimallee 14, D-14195 Berlin, Germany*

April 26, 2024

## Abstract

We develop an efficient method to calculate the third-order corrections to the self-energy of the hole-doped two-dimensional Hubbard model in space-time representation. Using the Dyson equation we evaluate the renormalized spectral function in various parts of the Brillouin zone and find significant modifications with respect to the second-order theory even for rather small values of the coupling constant  $U$ . The spectral function becomes unphysical for  $U \simeq W$ , where  $W$  is the half-width of the conduction band. Close to the Fermi surface and for  $U < W$ , the single-particle spectral weight is reduced in a finite energy interval around the Fermi energy. The increase of  $U$  opens a gap between the occupied and unoccupied parts of the spectral function.

## Introduction

The hole-doped two-dimensional (2-D) Hubbard model continues to attract considerable attention as it is believed to capture the essential features of “underdoped cuprates” [1]. In particular, the spectral properties of the model at small doping and the coupling strength  $U \geq 2W$ , where  $W$  is the half-width of the conduction band, are thought to be relevant for the angular resolved photoemission spectroscopy (ARPES) experiments. The ARPES data are used to study the frequency and momentum dependence of the single-particle excitations of 2-D electrons in  $CuO_2$  layers [2, 3] but the interpretation of the experimental results is quite difficult and often controversial. On the one hand, the observed spectral features do not fit any

simple conceptual framework; on the other hand, reliable theoretical results are not at hand. Thus, it is of interest to study in some detail the effect of correlation on the spectral function of the hole-doped 2-D Hubbard model.

The weak-coupling analysis of renormalized single-particle excitations has been presented in a number of papers [4]–[13], which treat  $U$  as an expansion parameter and consider the effects of correlation, doping, and temperature in various parts of the Brillouin zone. These papers show that correlation changes significantly the single-particle spectral properties even for relatively small values of  $U$ , and the results exhibit a number of interesting features which are also seen in cuprates. However, a quantitative comparison with the experimental data is difficult since most weak-coupling theories become unreliable for  $U \geq W$ .

The breakdown of the weak-coupling schemes based on truncated perturbation expansions is not immediately discernible from the spectral function, but is signalled for  $U \simeq W$  by the negative compressibility [12] and the rapid deviation of the Fermi volume  $v_F$  from the values required by the Luttinger theorem [14]. The theories based on an infinite summation of selected classes of diagrams [15, 16, 17] are also unreliable for large values of  $U$ , because they overemphasize the spectral weight of quasiparticle peaks and do not produce the Hubbard side-bands, which are typical of strong local correlations. Thus, the perturbational results obtained so far give some insights into the properties of the Hubbard model but do not allow a consistent description of correlated electrons at intermediate or large values of  $U$  which one needs to discuss the cuprates or make a comparison with the t-J model.

The weak-coupling approach to the Hubbard model poses a number of questions which should be considered if the results are to be extrapolated into the large- $U$  regime. What is the range of validity of the asymptotic  $U$  expansion? What is the importance of the terms that are neglected in the self-energy expansion? Is it possible to use a finite-order perturbation theory for the values of  $U$  such that the low-energy excitations of the Hubbard model and the t-J model look similar? Are the weak-coupling results obtained by perturbative methods representative of the strong-coupling limit? And finally, does the low-energy physics of the 2-D Hubbard model, as defined by some weak-coupling scheme, produce the right phenomenology for underdoped cuprates?

To answer these questions one would have to examine the general structure of the perturbation expansion or compare the weak-coupling solution with the exact one, which is not possible at present. Some insight, however, can be obtained by extending the perturbation expansion beyond the 2nd order and studying the stability of a truncated series with respect to higher-order corrections. Here, we calculate the momentum-dependent single-particle self-energy up to the 3rd order, and show that the individual 3rd-order diagrams are large but that the total 3rd-order contribution is much smaller than the 2nd-order one. This approximate mutual cancellation of 3rd-order diagrams holds for any doping and not just for zero doping, where it is a consequence of electron-hole symmetry.

Once the 3rd-order contribution becomes comparable to the 2nd-order one, which happens here for  $U \simeq W$ , the truncated perturbation series leads to unphysical results. In the “physical” range,  $U < W$ , we find a number of interesting

features which offer additional insight into the anomalies of the 2-D hole-doped Hubbard model. However, the error of neglecting the higher-order terms might become significant for larger values of  $U$  even within the physical range [18]. It would be interesting to see whether the 4th order contribution improves the perturbation theory and extends it to experimentally relevant values of  $U$ , or whether it renders the weak-coupling approach useless. The technical problems involved with such calculations are not much different from the problems encountered in the 3rd-order calculations [19]. The Matsubara summations for the 4th-order diagrams are straightforward, if tedious, and the 4th-order momentum summations follow from the same numerical strategies which solve the 3rd order. Thus, the 3rd-order calculations can be considered as a small but necessary step in our efforts to clarify the properties of the Hubbard model up to intermediate values of the coupling strength.

We should also remark that the accurate characterization of the weak-coupling regime might be of some interest for the approximate schemes which interpolate between the small- $U$  and the large- $U$  limit of the model. In the case of the infinite-dimensional Hubbard model and the single-impurity Anderson model, interpolations like that [20]–[23] come very close to the exact solution. However, on a 2-D lattice one deals with the anisotropic  $\mathbf{k}$  space, and the interpolation schemes might be difficult to construct.

The present paper is organized as follows. First the retarded 2nd- and 3rd-order self-energies are expressed in terms of multiple momentum integrals. Then we introduce the space-time representation and use the Fast Fourier Transform (FFT) algorithm to evaluate the self-energy as a function of energy for all points in the Brillouin zone. The relative importance of the 2nd- and 3rd-order terms obtained by FFT is analyzed and the stability of the weak-coupling solution is discussed. Next, the spectral properties of the model are calculated for low temperatures, for a given value of the chemical potential, and for various points in the Brillouin zone. Finally, the spectral features and their relevance for the experimental data are briefly discussed. The calculations are explained in detail in the Appendix.

## Calculations

To start with, the Hubbard Hamiltonian is written as

$$H = \sum_{i,j,\sigma} t_{ij} c_{i\sigma}^\dagger c_{j\sigma} - \mu' \sum_{i,\sigma} n_{i\sigma} + U \sum_{i=1}^{N_g} (n_{i\uparrow} - \langle\langle n_{i\uparrow} \rangle\rangle)(n_{i\downarrow} - \langle\langle n_{i\downarrow} \rangle\rangle) \quad , \quad (1)$$

where  $t_{ij}$  is the nearest-neighbor hopping integral,  $c_{i\sigma}$  ( $c_{i\sigma}^\dagger$ ) destroys (creates) an electron at site  $\mathbf{R}_i$  with spin  $\sigma$ ,  $n_{i\sigma} = c_{i\sigma}^\dagger c_{i\sigma}$  is the electron number operator,  $U$  is the local electron-electron interaction, and  $\langle\langle \dots \rangle\rangle$  denotes the ensemble average over the eigenstates of the *full* Hamiltonian (1). The parameter  $\mu' = \mu - \langle\langle n_{-\sigma} \rangle\rangle U$  is the “effective chemical potential”,  $\mu$  being the chemical potential proper. The energy of an unrenormalized single-particle excitation propagating with wave vector

$\mathbf{k}$ , counted from the Fermi level, is  $\omega_{\mathbf{k}}^0 = \epsilon_{\mathbf{k}} - \mu'$ , where  $\epsilon_{\mathbf{k}} = -2[t_x \cos(k_x a_x) + t_y \cos(k_y a_y)]$ . The Fermi momentum is denoted by  $\mathbf{k}_F$ . We consider the fluctuations above a mean-field-like paramagnetic state, in which the number of particles coincides with the exact particle number,  $\langle\langle n_{i\uparrow} \rangle\rangle = \langle\langle n_{i\downarrow} \rangle\rangle = n_e/2$ , and assume  $t_x = t_y = t$ , the half-bandwidth being  $W = 4t$ .

The self-energy diagrams are generated by the usual Matsubara imaginary-time perturbation expansion with respect to the last term in Eq. (1). All the 2nd- and 3rd-order diagrams are shown in Fig. 1, where the dashed line represents the local interaction ( $-U$ ) and the full line stands for the unperturbed propagator  $G_{\mathbf{k}}^0(i\omega_n) = (i\omega_n - \omega_{\mathbf{k}}^0)^{-1}$ , defined with the first two terms in Eq. (1). Note that there are no self-energy diagrams that are  $\mathbf{k}$  and  $\omega$  independent, the so-called one-legged diagrams. Because of the separation of the Hamiltonian as in (1), all one-legged diagrams of all orders add up to zero. Equivalently one could say that they have been hidden in the ‘‘effective chemical potential’’  $\mu' = \mu - \langle\langle n_{-\sigma} \rangle\rangle U$ .

The self-energy calculations for a finite lattice with periodic boundary conditions and a discretized time axis simplify considerably in the space-time representation [5]. The 2nd- and the 3rd-order *retarded* proper self-energy contributions are given by the expressions

$$\Sigma_{\mathbf{R}}^{(2)}(t) = -iU^2 \Theta(t) [a^2(\mathbf{R}, t) b^*(\mathbf{R}, t) + b^2(\mathbf{R}, t) a^*(\mathbf{R}, t)] \quad , \quad (2)$$

$$\begin{aligned} \Sigma_{\mathbf{R}}^{(3)}(t) = & U^3 \Theta(t) \{ [a(\mathbf{R}, t) w_1(\mathbf{R}, t) - b(\mathbf{R}, t) w_1^*(\mathbf{R}, t)] \\ & - [a^*(\mathbf{R}, t) w_2(\mathbf{R}, t) + b^*(\mathbf{R}, t) w_3(\mathbf{R}, t)] \} \quad , \quad (3) \end{aligned}$$

where  $a(\mathbf{R}, t)$  and  $b(\mathbf{R}, t)$  are the standard [24] double-time Green’s functions of  $H_0$ ,

$$a(\mathbf{R}, t) \equiv \langle c_{\mathbf{0}}^\dagger(0) c_{\mathbf{R}}(t) \rangle = \frac{1}{N} \sum_{\mathbf{k}} e^{i(\mathbf{k}\cdot\mathbf{R} - \omega_{\mathbf{k}}^0 t)} f(\omega_{\mathbf{k}}^0) \quad , \quad (4)$$

$$b(\mathbf{R}, t) \equiv \langle c_{\mathbf{R}}(t) c_{\mathbf{0}}^\dagger(0) \rangle = \frac{1}{N} \sum_{\mathbf{k}} e^{i(\mathbf{k}\cdot\mathbf{R} - \omega_{\mathbf{k}}^0 t)} f(-\omega_{\mathbf{k}}^0) \quad , \quad (5)$$

while the functions  $w_i(\mathbf{R}, t)$  are space-time convolutions of functions composed of products of  $a(\mathbf{R}, t)$ ’s and  $b(\mathbf{R}, t)$ ’s, given by expression (24) in the Appendix. Instead of evaluating these convolutions directly, we decouple them by a pair of Fourier transforms, as shown in (25). (The time variable  $t$  should not be confused with the hopping amplitude  $t$ .)

The *retarded* self-energy in the energy-momentum representation,  $\Sigma_{\mathbf{k}}(\omega) \equiv \Sigma_{\mathbf{k}}(\omega + i0^+)$ , is then given by the inverse Fourier transform

$$\Sigma_{\mathbf{k}}(\omega) = \sum_{\mathbf{R}} e^{-i\mathbf{k}\cdot\mathbf{R}} \int_0^\infty dt e^{i\omega t} [\Sigma_{\mathbf{R}}^{(2)}(t) + \Sigma_{\mathbf{R}}^{(3)}(t)] \quad . \quad (6)$$

The self-energy calculation is thus reduced to a sequence of Fourier transforms, which can be evaluated very efficiently by the FFT technique. In this paper we consider a lattice with  $N_g = 256 \times 256$  sites and define discretized momenta in the quadratic Brillouin zone as  $\mathbf{k} = (k_x, k_y)$ , where  $k_{x,y} = \Delta k(l_{x,y} - 1)$  with  $\Delta k = 2\pi/\sqrt{N_g}$  and  $l_{x,y} = 1, \dots, \sqrt{N_g}$ . The  $\Gamma$  point is at  $\mathbf{k} = (0, 0)$ , the X point at  $\mathbf{k} = (\pi, 0)$ , the M point at  $\mathbf{k} = (\pi/2, \pi/2)$ , and the Z point at  $\mathbf{k} = (\pi, \pi)$ .

Having found  $\Sigma_{\mathbf{k}}(\omega, T)$ , we calculate the spectral function  $A_{\mathbf{k}}(\omega, T)$  from the Dyson equation,

$$A_{\mathbf{k}}(\omega, T) = -\frac{1}{\pi} \text{Im} \frac{1}{\omega + i0^+ - \omega_{\mathbf{k}}^0 - \Sigma_{\mathbf{k}}(\omega, T)} \quad , \quad (7)$$

and obtain the renormalized density of states,

$$\rho(\omega, T) = \frac{1}{N} \sum_{\mathbf{k}} A_{\mathbf{k}}(\omega, T), \quad (8)$$

and the renormalized particle number,

$$n_e = 2 \int_{-\infty}^{\infty} d\omega f(\omega) \rho(\omega, T) \quad . \quad (9)$$

Eq. (9), together with Eqs. (8) and (7), establishes the functional dependence of the renormalized particle number  $n_e$  on the “effective chemical potential”  $\mu'$ , with  $U$  and  $T$  as parameters, everything scaled in units of  $W$ :

$$n_e = \mathcal{N}(\mu'/W; U/W, k_B T/W) \quad (10)$$

On the other hand, the pure chemical potential  $\mu$  is given by

$$\begin{aligned} \mu &= \mu' + \frac{U}{2} n_e \\ &= \mu' + \frac{U}{2} \mathcal{N}(\mu'/W; U/W, k_B T/W) \end{aligned} \quad (11)$$

Eqs. (10) and (11) establish the dependence of  $n_e$  on  $\mu$  or vice versa, with both quantities given parametrically as functions of  $\mu'$ . In this way one does not have to really *solve* Eq. (9) as a self-consistency *equation* for  $n_e(\mu)$ , it suffices to just *evaluate* Eqs. (10) and (11) for a number of close-lying values of  $\mu'$ .

One should note that the  $n$ -consistency is here forced upon the approximate proper self-energy,  $\Sigma_{\mathbf{k}}^{(2)}(\omega) + \Sigma_{\mathbf{k}}^{(3)}(\omega)$ , and can therefore be attained only approximately.

The peaks of  $A_{\mathbf{k}}(\omega)$  give the dispersion of quasiparticle excitations,  $\omega_{\mathbf{k}}$ ; the renormalized Fermi surface is defined by the set of points in the momentum space at which  $\omega_{\mathbf{k}} = 0$ . (At the Fermi surface,  $A_{\mathbf{k}}(\omega)$  has a singularity at the Fermi energy  $E_F$ .) According to the Luttinger theorem, the number of  $\mathbf{k}$  points enclosed by the Fermi surface (i.e. the Fermi volume  $v_F$ ) should coincide with  $n_e$ . In our approximate treatment, which is based on the 3rd-order self-energy and the Dyson equation, we find  $v_F > n_e$ , but the relative difference between  $v_F(U, \mu)$  and  $n_e(U, \mu)$  for  $U \leq W$  is very small.

In what follows, we first discuss  $\Sigma_{\mathbf{k}}(\omega, T)$  and then the ensuing spectral function, the density of states, the renormalized dispersion, and the Fermi surface of the model for the temperature  $k_B T = t/250$ ,  $U = 3.5t$ , and  $\mu' = 0.2t$ , which corresponds to  $n_e = 0.96$ . The same numerical program, available from the authors upon request, returns the self-energy in the irreducible wedge of the Brillouin zone for any other value of  $T$ ,  $U$ , and  $\mu$ .

## Results and discussion

In Figs. 2 and 3 we show the real and the imaginary part of  $\Sigma_{\mathbf{k}}^{(3)}(\omega)$ , respectively, plotted versus  $\omega$  for several momenta along the  $\Gamma$ -X-Z-M- $\Gamma$  cuts through the Brillouin zone. The dotted and the dashed-dotted lines show the two 3rd-order contributions,  $\Sigma_{\text{PH}}^{(3)}(\omega)$  and  $\Sigma_{\text{PP}}^{(3)}(\omega)$ , respectively, while the full line is their sum,  $\Sigma_{\mathbf{k}}^{(3)}(\omega)$ . The magnitudes of the individual 3rd-order contributions are about the same as the magnitude of  $\Sigma_{\mathbf{k}}^{(2)}(\omega)$  (see below and in Ref. [9]) but the total 3rd-order contribution is relatively small, except in a narrow frequency range where the approximate cancellation of electron-electron and electron-hole terms does not occur. This behavior indicates that the correct solution of the hole-doped model requires all 3rd-order diagrams, and can not be obtained by the partial summation of electron-electron or electron-hole diagrams.

The functional form of  $\Sigma_{\mathbf{k}}^{(3)}(\omega)$  is very much  $\mathbf{k}$ -dependent. Far off the Fermi surface  $\text{Im}\Sigma_{\mathbf{k}}^{(3)}(\omega)$  does not show much structure in the low-energy region and its slope around  $E_F$  is always small (see Figs. 3 and 5 for data corresponding to  $\Gamma$  and Z points). On the other hand, for  $\mathbf{k} \simeq \mathbf{k}_F$ ,  $\text{Im}\Sigma_{\mathbf{k}}^{(3)}(\omega)$  acquires a pronounced minimum at  $E_F$  (see Figs. 3 and 5 for data corresponding to X and M points). In the low-energy region, the  $\text{Im}\Sigma_{\mathbf{k}}^{(3)}(\omega)$  and  $\text{Im}\Sigma_{\mathbf{k}}^{(2)}(\omega)$  have opposite sign, and both vanish at  $E_F$  [25] with a zero slope.

The properties of the “full” self-energy,  $\Sigma_{\mathbf{k}}^{(2)}(\omega) + \Sigma_{\mathbf{k}}^{(3)}(\omega)$ , are summarized in Fig. 4, where  $\text{Im}\Sigma_{\mathbf{k}}(\omega)$  is plotted versus  $\omega$  for the same  $\mathbf{k}$ 's as in Fig. 3. The low-energy behavior at  $\Gamma$ , X, Z, and M is displayed in Fig. 5. For comparison, the individual 2nd- and 3rd-order contributions are shown as well. The low-energy features of the  $\text{Re}\Sigma_{\mathbf{k}}(\omega)$  are not changed much by the 3rd-order renormalization, regardless of  $\mathbf{k}$ . On the other hand, the low-energy properties of  $\text{Im}\Sigma_{\mathbf{k}}(\omega)$  are strongly influenced by the 3rd-order corrections. For example, close to X and M points, the 2nd- and the 3rd-order terms nearly cancel and make the low-energy part of  $\text{Im}\Sigma_{\mathbf{k}}(\omega)$  rather flat in an extended interval around  $E_F$ . The relative contribution of

the 2nd- and the 3rd-order terms depends on the coupling strength and for a given  $\mu$  there is always a critical correlation  $U_c(\mu, \mathbf{k}_c)$  such that the coefficient of the  $\omega^2$  term in  $\text{Im}\Sigma_{\mathbf{k}_c}(\omega)$  vanishes at some  $\mathbf{k}_c$ . For  $U < U_c$  the curvature of  $\text{Im}\Sigma_{\mathbf{k}}(\omega)$  at  $E_F$  is negative for all  $\mathbf{k}$  and the ensuing spectral weight is always positive. However, for  $U > U_c$  the curvature of  $\text{Im}\Sigma_{\mathbf{k}}(\omega)$  at  $E_F$  becomes positive at some points in the Brillouin zone, and the corresponding spectral weight becomes negative. This behavior indicates that the 3rd-order  $U$  expansion breaks down for  $U \simeq W$ , and that  $\Sigma_{\mathbf{k}}^{(2)}(\omega)$  provides an accurate renormalization for small values of  $U$  only.

For  $U$  close to but less than  $U_c$ , the curvature of  $\text{Im}\Sigma_{\mathbf{k}}(\omega)$  at  $E_F$  is found to be the smallest for  $\mathbf{k} \simeq \mathbf{k}_F$ . Thus, in the presence of correlations the Fermi surface properties assume qualitatively new features due to the  $\omega^3$  and higher-order self-energy terms. Unfortunately, these non-Fermi-liquid (NFL) features require large values of  $U$  and can not be properly discussed without the higher-order terms in the expansion. Leaving the 4th-order renormalization for future studies [19], we consider here the 3rd-order renormalization and discuss spectral properties for  $U < U_c \simeq W$ .

The variation of  $A_{\mathbf{k}}(\omega)$  along  $\Gamma \rightarrow X$ ,  $X \rightarrow Z$  and  $Z \rightarrow \Gamma$  cuts in the Brillouin zone is shown in Fig. 6. The 3rd-order spectral function, like the 2nd-order one [9], assumes at all wave vectors a typical shape with a low-energy quasiparticle peak and a high-energy incoherent background. The correlation reduces the quasiparticle spectral weight and enhances the incoherent background of  $A_{\mathbf{k}}(\omega)$ . However, for  $U = 3.5t$  and  $n_e = 0.96$  the transfer of spectral weight out of the low-energy region is small, and the quasiparticle peak is not fully separated from the incoherent background, except for  $\mathbf{k}$ 's which are far off the Fermi surface. At the Fermi surface, the singular quasiparticle peak can be represented as  $A_{\mathbf{k}_F}(\omega) = Z_{\mathbf{k}_F} \delta(\omega - E_F)$ , where  $Z_{\mathbf{k}}$  describes the reduction of the quasiparticle weight due to self-energy corrections. For  $\mathbf{k} \neq \mathbf{k}_F$  the quasiparticle peak broadens, becomes asymmetric, and attains a maximum at some finite frequency. The asymmetry of  $A_{\mathbf{k}}(\omega)$  is caused by an incoherent background, which slows down the high- $\omega$  decay, and the NFL behavior at small  $\omega$ . A new feature due to the 3rd-order, which begins to emerge for  $U \simeq W$ , is the suppression of spectral weight in a finite energy interval around  $E_F$ . For  $\mathbf{k} \simeq \mathbf{k}_F$ , the singular quasiparticle peak at the Fermi energy is separated from the occupied and unoccupied incoherent states by a pseudogap. For  $\mathbf{k} < \mathbf{k}_F$  a real gap appears between the (occupied) quasiparticle peak and the (unoccupied) incoherent states. (The small background seen in the numerical data is due to the damping factor used for the real-axis propagators.)

The renormalized quasiparticle dispersion,  $\omega_{\mathbf{k}}$ , is obtained by tracing the maximum of  $A_{\mathbf{k}}(\omega)$  across several cuts in the momentum space and is shown in Fig. 7. Circles show  $\omega_{\mathbf{k}}$  and full line gives the unrenormalized dispersion,  $\omega_{\mathbf{k}}^0$ , for the same number of particles. Correlation reduces the overall width of the quasiparticle band and extends the flat dispersion around  $(\pi, 0)$ . Essentially the same dispersion is obtained by solving the secular equation

$$\omega_{\mathbf{k}}(T) - (\epsilon_{\mathbf{k}} - \mu') - \Sigma_{\mathbf{k}}[\omega_{\mathbf{k}}(T), T] = 0 \quad . \quad (12)$$

The inspection of Figs. 6 or 7 shows that the M-point quasiparticle peak is somewhat above  $E_F$ , while the X-point peak is right at  $E_F$ . Thus, the renormalized Fermi surface, defined by the set of  $\mathbf{k}$  points such that the quasiparticle peak is at  $E_F$ , has a different topology than the non-interacting Fermi surface with the same number of holes. The renormalized Fermi surface resembles the tight-binding result which adds to  $t_{ij}$  the next-nearest-neighbor hopping  $t'_{ij}$ .

The renormalized density of states  $\rho(\omega)$  calculated for  $U = 3.5t$  and  $n_e = 0.96$  is plotted in Fig. 8 as a function of  $\omega$ . The transfer of the low-energy spectral weight out of the low- $\omega$  region is clearly seen but  $U \leq W$  is not sufficient to generate the incoherent Hubbard side-bands. The density of states at  $E_F$  is not much enhanced from the unperturbed value despite the reduced dispersion, because the quasiparticle weight is reduced by  $Z_{\mathbf{k}}$ . One has a metal but a strange one.

In summary, we developed an efficient method to perform the momentum summations in the self-energy expansion for the hole-doped 2-D Hubbard model and evaluated the coefficients of the  $U^2$  and the  $U^3$  terms. The third-order corrections lead to additional anisotropy and asymmetry of the spectral function and give rise to new features with respect to the 2nd-order renormalization. For large enough  $U$  we find strong reduction of the single-particle spectral weight around  $E_F$ . The quasiparticle dispersion is also reduced and the saddle point singularities are extended. The Fermi surface obtained by the 3rd-order renormalization for a hole-doped system is closed around the Z point. At the Fermi surface, the quasiparticle peak and the incoherent background are separated by a pseudogap. Off the Fermi surface we find a finite region of negligible spectral weight between the quasiparticle peak and the Fermi energy. This behavior hints to a possible scenario in which the system is metallic with a narrow Kondo-like resonance at the Fermi energy, and a pseudogap for incoherent excitations. However, the anomalous spectral features which we obtain here are due to the cancellation of the 2nd- and the 3rd-order self-energy terms, and the stability of this result with respect to the 4th-order renormalization remains to be seen. The 3rd-order perturbation expansion shows that the solution of the hole-doped model can not be obtained by partial summation of diagrams, and that the properties inferred from the 2nd-order theory seem to be qualitatively correct for  $U \leq W$  only.

## Appendix

Carrying out the Matsubara summations over Fermi frequencies and continuing analytically the result from the discrete points on the imaginary axis onto the complex plane, we find

$$\Sigma_{\mathbf{k}}^{(2)}(z) = \left(\frac{U}{N}\right)^2 \sum_{\mathbf{k}_1, \mathbf{k}_2} \frac{P(\omega_{\mathbf{k}-\mathbf{k}_1}^0, \omega_{\mathbf{k}_1-\mathbf{k}_2}^0, \omega_{\mathbf{k}_2}^0)}{z - (\omega_{\mathbf{k}-\mathbf{k}_1}^0 + \omega_{\mathbf{k}_1-\mathbf{k}_2}^0 - \omega_{\mathbf{k}_2}^0)} . \quad (13)$$

The third-order self-energy  $\Sigma_{\mathbf{k}}^{(3)}(z)$  comprises two diagrams, a particle-hole one and a particle-particle one,

$$\Sigma_{\mathbf{k}}^{(3)}(z) = \Sigma_{\text{PH}}^{(3)}(\mathbf{k}, z) + \Sigma_{\text{PP}}^{(3)}(\mathbf{k}, z) , \quad (14)$$

where

$$\begin{aligned} \Sigma_{\text{PH}}^{(3)}(\mathbf{k}, z) = & 2 \left( \frac{U}{N} \right)^3 \sum_{\mathbf{k}_1, \mathbf{k}_2, \mathbf{k}_3} \frac{P(\omega_{\mathbf{k}-\mathbf{k}_1}^0, -\omega_{\mathbf{k}_1-\mathbf{k}_2}^0, \omega_{\mathbf{k}_2}^0)}{z - (\omega_{\mathbf{k}-\mathbf{k}_1}^0 - \omega_{\mathbf{k}_1-\mathbf{k}_2}^0 + \omega_{\mathbf{k}_2}^0)} \\ & \times \frac{Q(-\omega_{\mathbf{k}_1-\mathbf{k}_3}^0, \omega_{\mathbf{k}_3}^0)}{(\omega_{\mathbf{k}_1-\mathbf{k}_3}^0 - \omega_{\mathbf{k}_3}^0) - (\omega_{\mathbf{k}_1-\mathbf{k}_2}^0 - \omega_{\mathbf{k}_2}^0)} , \end{aligned} \quad (15)$$

while the analogous expression for  $\Sigma_{\text{PP}}^{(3)}(\mathbf{k}, z)$  is obtained from  $-\Sigma_{\text{PH}}^{(3)}(\mathbf{k}, z)$  by changing the sign of three  $\omega_{\mathbf{k}}^0$ 's out of five, viz.  $\omega_{\mathbf{k}-\mathbf{k}_1}^0$ ,  $\omega_{\mathbf{k}_1-\mathbf{k}_2}^0$ , and  $\omega_{\mathbf{k}_1-\mathbf{k}_3}^0$ , everything else being the same as in (15). The functions P and Q are defined as

$$P(\epsilon_1, \epsilon_2, \epsilon_3) = f(\epsilon_1) f(\epsilon_2) f(\epsilon_3) + f(-\epsilon_1) f(-\epsilon_2) f(-\epsilon_3) ,$$

$$Q(\epsilon_1, \epsilon_2) = f(\epsilon_1) f(\epsilon_2) - f(-\epsilon_1) f(-\epsilon_2) ,$$

$f(\epsilon) = (e^{\beta\epsilon} + 1)^{-1}$  is the Fermi function, with  $\beta = 1/k_B T$ , and  $\omega_{\mathbf{k}}^0 = \epsilon_{\mathbf{k}} - \mu'$ .

The above equations are not suitable for numerical evaluation of  $\Sigma_{\mathbf{k}}^{(2)}(\omega \pm i0^+)$  and  $\Sigma_{\mathbf{k}}^{(3)}(\omega \pm i0^+)$  because of two reasons. First, one would have to deal with four-dimensional and six-dimensional integrations in  $\mathbf{k}$  space, respectively. Also, the denominators in expressions (13) and (15) vanish along various closed contours in  $\mathbf{k}$  space. The multiple integrals are therefore defined by their principal values and their evaluation requires a dense grid in  $\mathbf{k}$  space, which makes the numerical procedures very time-consuming.

The second- and third-order self-energies, given by Eqs. (13) – (15), are therefore transformed here from the energy-momentum to the space-time representation, which allows an accurate and efficient evaluation by the FFT algorithm.

In order to establish transparent shorthand notation, we first define the Fourier transforms as the operators

$$\mathcal{F}_{\mathbf{k} \rightarrow \mathbf{R}}[\dots] \equiv \frac{1}{N} \sum_{\mathbf{k}} e^{i\mathbf{k} \cdot \mathbf{R}} \dots ,$$

$$\mathcal{F}_{\omega \rightarrow t}[\dots] \equiv \int_{-\infty}^{\infty} \frac{d\omega}{2\pi} e^{-i\omega t} \dots ,$$

as well as the inverse transforms

$$\mathcal{F}_{\mathbf{k} \rightarrow \mathbf{R}}^{-1}[\dots] \equiv \sum_{\mathbf{R}} e^{-i\mathbf{k} \cdot \mathbf{R}} \dots ,$$

$$\mathcal{F}_{\omega \rightarrow t}^{-1}[\dots] \equiv \int_{-\infty}^{\infty} dt e^{i\omega t} \dots .$$

We also introduce shorthand for four-dimensional transforms

$$\mathcal{F} \equiv \mathcal{F}_{\mathbf{k} \rightarrow \mathbf{R}} \mathcal{F}_{\omega \rightarrow t} \quad \text{and} \quad \mathcal{F}^{-1} \equiv \mathcal{F}_{\mathbf{k} \rightarrow \mathbf{R}}^{-1} \mathcal{F}_{\omega \rightarrow t}^{-1} .$$

The retarded/advanced self-energy in space-time representation is then defined as

$$\Sigma_{r/a}(\mathbf{R}, t) = \mathcal{F} [\Sigma_{\mathbf{k}}(\omega \pm i0^+)] .$$

For the 2nd-order self-energy we start from the expression (13) for  $\Sigma_{\mathbf{k}}^{(2)}(\omega \pm i0^+)$  and first evaluate the  $\omega \rightarrow t$  Fourier transform. Using the relation

$$\mathcal{F}_{\omega \rightarrow t} \left[ \frac{1}{\omega \pm i\delta - \epsilon} \right] = \mp i \Theta(\pm t) e^{-i(\epsilon \mp i\delta)t} ,$$

which holds for any  $\delta > 0$ , we factorize the denominator in (13) into a product of three exponentials and find

$$\Sigma_{r/a}^{(2)}(\mathbf{R}, t) = \mp i U^2 \Theta(\pm t) \mathcal{F}_{\mathbf{k} \rightarrow \mathbf{R}} \left[ S_{\mathbf{k}}^{(2)}(t) \right] , \quad (16)$$

where  $S_{\mathbf{k}}^{(2)}(t)$  denotes the double convolution in momentum space,

$$\begin{aligned} S_{\mathbf{k}}^{(2)}(t) &= \frac{1}{N^2} \sum_{\mathbf{k}_1, \mathbf{k}_2} [A(\mathbf{k} - \mathbf{k}_1, t) A(\mathbf{k}_1 - \mathbf{k}_2, t) B^*(\mathbf{k}_2, t) \\ &\quad + B(\mathbf{k} - \mathbf{k}_1, t) B(\mathbf{k}_1 - \mathbf{k}_2, t) A^*(\mathbf{k}_2, t)] , \end{aligned}$$

with functions  $A(\mathbf{k}, t)$  and  $B(\mathbf{k}, t)$  defined as

$$A(\mathbf{k}, t) = e^{-i\omega_{\mathbf{k}}^0 t} f(\omega_{\mathbf{k}}^0) , \quad (17)$$

$$B(\mathbf{k}, t) = e^{-i\omega_{\mathbf{k}}^0 t} f(-\omega_{\mathbf{k}}^0) . \quad (18)$$

Recalling that the Fourier transform of a convolution can be expressed as a product of Fourier transforms of the integrands, we write  $A(\mathbf{k}, t)$  and  $B(\mathbf{k}, t)$  as

$$A(\mathbf{k}, t) = \mathcal{F}_{\mathbf{k} \rightarrow \mathbf{R}}^{-1} [a(\mathbf{R}, t)] \quad , \quad (19)$$

$$B(\mathbf{k}, t) = \mathcal{F}_{\mathbf{k} \rightarrow \mathbf{R}}^{-1} [b(\mathbf{R}, t)] \quad , \quad (20)$$

and disentangle the double convolution  $S_{\mathbf{k}}^{(2)}(t)$  as

$$S_{\mathbf{k}}^{(2)}(t) = \mathcal{F}_{\mathbf{k} \rightarrow \mathbf{R}}^{-1} [a^2(\mathbf{R}, t) b^*(\mathbf{R}, t) + b^2(\mathbf{R}, t) a^*(\mathbf{R}, t)] \quad .$$

Inserted in expression (16) this gives

$$\Sigma_{r/a}^{(2)}(\mathbf{R}, t) = \mp i U^2 \Theta(\pm t) [a^2(\mathbf{R}, t) b^*(\mathbf{R}, t) + b^2(\mathbf{R}, t) a^*(\mathbf{R}, t)] \quad . \quad (21)$$

In short,  $\mathcal{F}_{\omega \rightarrow t}$  yields a convolution in  $\mathbf{k}$  space, while  $\mathcal{F}_{\mathbf{k} \rightarrow \mathbf{R}}$  disentangles this convolution into a product.

As regards the third-order self-energy, we proceed in the same way, starting from expression (15) for  $\Sigma_{\text{PH}}^{(3)}(\mathbf{k}, z)$ . As before, the  $\omega \rightarrow t$  Fourier transform factorizes the  $z$ -dependent term in the denominator, but the  $\mathbf{k}$  summations still do not represent a convolution due to the presence of the unfactorized singular term  $1/(\omega_{\mathbf{k}_1 - \mathbf{k}_3}^0 - \omega_{\mathbf{k}_3}^0 - \omega_{\mathbf{k}_1 - \mathbf{k}_2}^0 + \omega_{\mathbf{k}_2}^0)$ . To factorize this term as well, we make use of the identity

$$\frac{1}{\epsilon} = \frac{1}{2} \lim_{\delta \rightarrow 0^+} \left( \frac{1}{\epsilon + i\delta} + \frac{1}{\epsilon - i\delta} \right) \quad ,$$

which holds for any  $\epsilon \neq 0$ , and

$$\frac{1}{\epsilon \pm i\delta} = \frac{1}{i} \int_0^{\pm\infty} dt e^{i(\epsilon \pm i\delta)t} \quad ,$$

which holds for any  $\delta > 0$ , to represent  $1/\epsilon$  as

$$\frac{1}{\epsilon} = \frac{1}{2i} \int_{-\infty}^{\infty} dt s(t) e^{i\epsilon t} \quad , \quad (22)$$

$$s(t) \equiv \text{sgn}(t) e^{-0^+|t|} \quad .$$

It is clear that (22) factorizes the above awkward term into a product of four exponentials. Altogether we obtain

$$\Sigma_{\text{PH}}^{(3)}(\mathbf{R}, t) = \pm \Theta(\pm t) U^3 \int_{-\infty}^{\infty} dt' s(t') \mathcal{F}_{\mathbf{k} \rightarrow \mathbf{R}} \left[ S_{\text{PH}}^{(3)}(\mathbf{k}, t, t') \right] ,$$

where the upper (lower) sign refers to the retarded (advanced) quantity, respectively, and  $S_{\text{PH}}^{(3)}(\mathbf{k}, t, t')$  denotes the triple  $\mathbf{k}$ -space convolution

$$\begin{aligned} S_{\text{PH}}^{(3)}(\mathbf{k}, t, t') &= \frac{1}{N^3} \sum_{\mathbf{k}_1, \mathbf{k}_2, \mathbf{k}_3} [A(\mathbf{k} - \mathbf{k}_1, t) B^*(\mathbf{k}_1 - \mathbf{k}_2, t - t') A(\mathbf{k}_2, t - t') \\ &\quad + B(\mathbf{k} - \mathbf{k}_1, t) A^*(\mathbf{k}_1 - \mathbf{k}_2, t - t') B(\mathbf{k}_2, t - t')] \\ &\quad \times [A^*(\mathbf{k}_1 - \mathbf{k}_3, t') B(\mathbf{k}_3, t') - B^*(\mathbf{k}_1 - \mathbf{k}_3, t') A(\mathbf{k}_3, t')] . \end{aligned}$$

The particle-particle third-order term  $\Sigma_{\text{PP}}^{(3)}(\mathbf{k}, z)$  is obtained from  $-\Sigma_{\text{PH}}^{(3)}(\mathbf{k}, z)$  by changing the sign of three  $\omega_{\mathbf{k}}^0$ 's out of five, viz.  $\omega_{\mathbf{k}-\mathbf{k}_1}^0$ ,  $\omega_{\mathbf{k}_1-\mathbf{k}_2}^0$ , and  $\omega_{\mathbf{k}_1-\mathbf{k}_3}^0$ . Since it is obvious from the above definitions (17) and (18) of  $A(\mathbf{k}, t)$  and  $B(\mathbf{k}, t)$  that  $\omega_{\mathbf{k}}^0 \rightarrow -\omega_{\mathbf{k}}^0$  implies  $A(\mathbf{k}, t) \leftrightarrow B^*(\mathbf{k}, t)$ , one obtains  $S_{\text{PP}}^{(3)}(\mathbf{k}, t, t')$  from  $-S_{\text{PH}}^{(3)}(\mathbf{k}, t, t')$  by the appropriate replacements of those A's and B's that have  $\mathbf{k} - \mathbf{k}_1$ ,  $\mathbf{k}_1 - \mathbf{k}_2$ , and  $\mathbf{k}_1 - \mathbf{k}_3$  as their arguments:

$$\begin{aligned} S_{\text{PP}}^{(3)}(\mathbf{k}, t, t') &= -\frac{1}{N^3} \sum_{\mathbf{k}_1, \mathbf{k}_2, \mathbf{k}_3} [B^*(\mathbf{k} - \mathbf{k}_1, t) A(\mathbf{k}_1 - \mathbf{k}_2, t - t') A(\mathbf{k}_2, t - t') \\ &\quad + A^*(\mathbf{k} - \mathbf{k}_1, t) B(\mathbf{k}_1 - \mathbf{k}_2, t - t') B(\mathbf{k}_2, t - t')] \\ &\quad \times [B(\mathbf{k}_1 - \mathbf{k}_3, t') B(\mathbf{k}_3, t') - A(\mathbf{k}_1 - \mathbf{k}_3, t') A(\mathbf{k}_3, t')] . \end{aligned}$$

Expressing  $A(\mathbf{k}, t)$  and  $B(\mathbf{k}, t)$  in terms of their Fourier transforms, Eqs. (19) and (20), as before, we decouple the above momentum-space convolutions and get

$$\begin{aligned} \Sigma_{r/a}^{(3)}(\mathbf{R}, t) &= \pm U^3 \Theta(\pm t) \{ [a(\mathbf{R}, t) w_1(\mathbf{R}, t) - b(\mathbf{R}, t) w_1^*(\mathbf{R}, t)] \\ &\quad - [a^*(\mathbf{R}, t) w_2(\mathbf{R}, t) + b^*(\mathbf{R}, t) w_3(\mathbf{R}, t)] \} , \end{aligned} \quad (23)$$

where the functions  $w_i(\mathbf{R}, t)$  are now given in the form of space-time convolutions

$$w_i(\mathbf{R}, t) = \sum_{\mathbf{R}'} \int_{-\infty}^{\infty} dt' g_i(\mathbf{R} - \mathbf{R}', t - t') h_i(\mathbf{R}', t') , \quad (24)$$

with  $g_i(\mathbf{R}, t)$  and  $h_i(\mathbf{R}, t)$  defined as

$$\begin{aligned}
g_1(\mathbf{R}, t) &= a(\mathbf{R}, t) b^*(\mathbf{R}, t) \ , \\
g_2(\mathbf{R}, t) &= b^2(\mathbf{R}, t) \ , \\
g_3(\mathbf{R}, t) &= a^2(\mathbf{R}, t) \ , \\
h_1(\mathbf{R}, t) &= s(t) [g_1^*(\mathbf{R}, t) - g_1(\mathbf{R}, t)] \ , \\
h_2(\mathbf{R}, t) &= s(t) [g_2(\mathbf{R}, t) - g_3(\mathbf{R}, t)] \ , \\
h_3(\mathbf{R}, t) &= h_2(\mathbf{R}, t) \ .
\end{aligned}$$

For the 3rd order we thus need two more Fourier transforms than for the 2nd order, to decouple these additional space-time convolutions as well:

$$w_i(\mathbf{R}, t) = \mathcal{F} \{ \mathcal{F}^{-1} [g_i(\mathbf{R}, t)] \cdot \mathcal{F}^{-1} [h_i(\mathbf{R}, t)] \} \ . \quad (25)$$

So, in order to obtain the  $n$ th-order self-energy  $\Sigma_{\mathbf{k}}^{(n)}(\omega \pm i0^+)$  via its space-time representation  $\Sigma_{r/a}^{(n)}(\mathbf{R}, t)$  using the FFT technique, we first calculate the quantities

$$a(\mathbf{R}, t) = \mathcal{F}_{\mathbf{k} \rightarrow \mathbf{R}} [A(\mathbf{k}, t)] = \frac{1}{N} \sum_{\mathbf{k}} e^{i(\mathbf{k} \cdot \mathbf{R} - \omega_{\mathbf{k}}^0 t)} f(\omega_{\mathbf{k}}^0) \ , \quad (26)$$

$$b(\mathbf{R}, t) = \mathcal{F}_{\mathbf{k} \rightarrow \mathbf{R}} [B(\mathbf{k}, t)] = \frac{1}{N} \sum_{\mathbf{k}} e^{i(\mathbf{k} \cdot \mathbf{R} - \omega_{\mathbf{k}}^0 t)} f(-\omega_{\mathbf{k}}^0) \ , \quad (27)$$

which requires performing the Fourier transform  $\mathcal{F}_{\mathbf{k} \rightarrow \mathbf{R}}$ . Then we proceed to evaluate  $\Sigma_{r/a}^{(n)}(\mathbf{R}, t)$ . For the 2nd order this amounts just to forming products of  $a(\mathbf{R}, t)$ 's and  $b(\mathbf{R}, t)$ 's, according to expression (21). For the 3rd order we first form functions  $g_i(\mathbf{R}, t)$  and  $h_i(\mathbf{R}, t)$ , again given by products of  $a(\mathbf{R}, t)$ 's and  $b(\mathbf{R}, t)$ 's, then perform a pair of Fourier transforms ( $\mathcal{F}^{-1}, \mathcal{F}$ ), to calculate functions  $w_i(\mathbf{R}, t)$  according to (25), and finally form  $\Sigma_{r/a}^{(3)}(\mathbf{R}, t)$  according to expression (23). Having thus found the self-energy in space-time representation, we apply  $\mathcal{F}^{-1}$  once again to get

$$\Sigma_{\mathbf{k}}^{(n)}(\omega \pm i0^+) = \mathcal{F}^{-1} \left[ \Sigma_{r/a}^{(n)}(\mathbf{R}, t) \right] \ .$$

The numerical problem involving space-time to momentum-frequency transformations (and vice versa) is solved by considering a finite lattice with periodic boundary conditions and discretizing the time axis. Here we take  $256 \times 256$  lattice sites and 1024 time points. As regards the  $\mathbf{k} \leftrightarrow \mathbf{R}$  transformation, the FFT is an exact procedure, while the  $t \leftrightarrow \omega$  transformation involves approximating the con-

tinuous Laplace transform with the corresponding discrete FFT. It would be *much* more time consuming to evaluate the space-time convolutions directly.

The 4th-order self-energy  $\Sigma_{\mathbf{k}}^{(4)}(z)$  comprises twelve topologically nonequivalent diagrams, nine of which are numerically different. However, only four out of these nine can be treated entirely along the same lines as those of the 2nd and 3rd order, i.e. completely decoupled and evaluated by a series of Fourier transforms alone. The remaining five do not yield multiple space-time convolutions, but double integrals instead, which can be only partly decoupled by Fourier transforms. The 4th order thus introduces new numerical difficulties, but tractable ones. The FFT can not do the whole job, but it does all steps but one.

The functions  $a(\mathbf{R}, t)$  and  $b(\mathbf{R}, t)$ , the building blocks of  $\Sigma_{r/a}^{(n)}(\mathbf{R}, t)$ , have a clear physical interpretation as double-time correlation functions

$$a(\mathbf{R}, t) = \langle c_{\mathbf{0}}^{\dagger}(0) c_{\mathbf{R}}(t) \rangle ,$$

$$b(\mathbf{R}, t) = \langle c_{\mathbf{R}}(t) c_{\mathbf{0}}^{\dagger}(0) \rangle ,$$

which can be shown by a straightforward evaluation of these thermal averages over the eigenstates of  $H_0$ , which gives (26) and (27). This relates them to the unperturbed Green's functions in space-time representation, viz. the retarded/advanced one,

$$\begin{aligned} G_{r/a}^0(\mathbf{R}, t) &= \mp i \Theta(\pm t) \langle [c_{\mathbf{0}}^{\dagger}(0), c_{\mathbf{R}}(t)]_+ \rangle \\ &= \mp i \Theta(\pm t) [b(\mathbf{R}, t) + a(\mathbf{R}, t)] , \end{aligned}$$

and the causal one,

$$\begin{aligned} G^0(\mathbf{R}, t) &= -i \langle T\{c_{\mathbf{R}}(t) c_{\mathbf{0}}^{\dagger}(0)\} \rangle \\ &= -i [\Theta(t) b(\mathbf{R}, t) - \Theta(-t) a(\mathbf{R}, t)] . \end{aligned}$$

It is clear that  $b(\mathbf{R}, t)$  is the probability amplitude for an electron to be created at  $\mathbf{R} = \mathbf{0}$  and  $t = 0$ , to propagate to the site  $\mathbf{R}$  which is reached at a later time  $t$ , and to be destructed at  $(\mathbf{R}, t)$ . This newly created electron is “composed of” the unoccupied (i.e., still available)  $\mathbf{k}$  states, as indicated by the amplitudes  $f(-\omega_{\mathbf{k}}^0) = 1 - f(\omega_{\mathbf{k}}^0)$  in the defining relation (27). In the same way  $a(\mathbf{R}, t)$  effectively describes the propagation of a hole created at  $(\mathbf{R}, t < 0)$  and destructed at  $(\mathbf{R} = \mathbf{0}, t = 0)$ .

## Acknowledgments

This work has been financially supported by the Alexander von Humboldt Foundation, the Sonderforschungsbereich 166 Duisburg/Bochum, and the National Science Foundation under grant DMR-9973225.

## References

- [1] P.W. Anderson, *The Theory of Superconductivity in the High  $T_c$  Cuprates* (Princeton University Press, Princeton, New Jersey, 1997).
- [2] T. Valla, A. V. Fedorov, P. D. Johnson, B. O. Wells, S. L. Hulbert, Q. Li, G. D. Gu, and N. Koshizuka, *Science* **285**, 2110 (1999).
- [3] A. Kaminski, J. Mesot, H. Fretwell, J. C. Campuzano, M. R. Norman, M. Randeria, H. Ding, T. Sato, T. Takahashi, T. Mochiku, K. Kadowaki, and H. Hoehst, *Phys. Rev. Lett.* **84**, 1788 (2000).
- [4] A. Virosztek and J. Ruvalds, *Phys. Rev. B* **42**, 4064 (1990).
- [5] H. Schweitzer and G. Czycholl, *Z. Phys. B* **83**, 93 (1991).
- [6] V. Zlatić, B. Horvatić, G. Schliecker and K.-D. Schotte, *Phil. Mag. B* **65**, 1255 (1992).
- [7] J. Galán, J. A. Vergés, and A. Martín-Rodero, *Phys. Rev. B* **48**, 13654 (1993).
- [8] C. J. Rodes and R. L. Jacobs, *J. Phys. Cond. Matter* **5**, 5649 (1993).
- [9] V. Zlatić, K.-D. Schotte and G. Schliecker, *Phys. Rev. B* **52**, 3639 (1995).
- [10] T. Hotta and S. Fujimoto, *Phys. Rev. B* **54**, 5381 (1996).
- [11] V. Zlatić, P. Entel and S. Grabowski, *Europhys. Letters* **34**, 693 (1996).
- [12] V. Zlatić, S. Grabowski and P. Entel, *Phys. Rev. B* **56**, 14875 (1997).
- [13] S. Yoda and K. Yamada, *Phys. Rev. B* **60**, 7886 (1999).
- [14] C. J. Halboth and W. Metzner, *Z. Phys. B* **102**, 501 (1997).
- [15] H. Fukuyama, Y. Hasegawa, and O. Narikiyo, *J. Phys. Soc. Jpn.* **60**, 2013 (1991).
- [16] J. R. Engelbrecht and M. Randeria, *Phys. Rev. B* **45**, 12419 (1992).
- [17] M. Langer, J. Schmalian, S. Grabowski, and K. H. Bennemann *Phys. Rev. Lett.* **75**, 4508 (1995).
- [18] This could be due to three unfavourable possibilities: (i) the expansion might be an asymptotic one, and therefore irrelevant for any value of  $U$  except  $U \rightarrow 0$ ; (ii) the expansion might be convergent, but the radius of convergence might be exceeded; (iii) even within the radius of convergence the series might converge very slowly.
- [19] B. Horvatić and V. Zlatić, unpublished

- [20] A. Martín-Rodero, F. Flores, M. Baldo, and R. Pucci, *Solid State Commun.* **44**, 911 (1982).
- [21] A. Martín-Rodero, E. Louis, F. Flores and C. Tejedor, *Phys. Rev. B* **29**, 476 (1984); *Phys. Rev. B* **33**, 1814 (1986).
- [22] J. Ferrer, A. Martín-Rodero, and F. Flores, *Phys. Rev. B* **36**, 6149 (1987).
- [23] H. Kajueter and G. Kotliar, *Phys. Rev. Lett.* **77**, 131 (1996).
- [24] L. Kadanoff and G. Baym, *Quantum Statistical Mechanics*, Benjamin, New York, 1962.
- [25] The small shift seen in the numerical data for some  $\mathbf{k}$  points is caused by the damping factor in the unperturbed propagators, which is introduced to speed up the calculations.

## Figure captions

Fig. 1. Diagrammatic representation of second- and third-order self-energy contributions.

Fig. 2. Real part of  $\Sigma_{\mathbf{k}}^{(3)}(\omega)$  along the  $\Gamma \rightarrow X$ ,  $X \rightarrow Z$ , and  $Z \rightarrow \Gamma$  cuts through the Brillouin zone.  $\text{Re } \Sigma_{\text{PH}}^{(3)}$ ,  $-\text{Re } \Sigma_{\text{PP}}^{(3)}$ , and  $\text{Re } \Sigma^{(3)} = \text{Re } \Sigma_{\text{PH}}^{(3)} + \text{Re } \Sigma_{\text{PP}}^{(3)}$  are represented by dashed, dashed-dotted, and full lines, respectively.

Fig. 3. Imaginary part of  $\Sigma_{\mathbf{k}}^{(3)}(\omega)$  along the  $\Gamma \rightarrow X$ ,  $X \rightarrow Z$ , and  $Z \rightarrow \Gamma$  cuts through the Brillouin zone.  $\text{Im } \Sigma_{\text{PH}}^{(3)}$ ,  $-\text{Im } \Sigma_{\text{PP}}^{(3)}$ , and  $\text{Im } \Sigma^{(3)} = \text{Im } \Sigma_{\text{PH}}^{(3)} + \text{Im } \Sigma_{\text{PP}}^{(3)}$  are represented by dashed, dashed-dotted, and full lines, respectively.

Fig. 4. Imaginary parts of  $\Sigma_{\mathbf{k}}^{(2)}(\omega)$  and  $\Sigma_{\mathbf{k}}^{(3)}(\omega)$  along the  $\Gamma \rightarrow X$ ,  $X \rightarrow Z$ , and  $Z \rightarrow \Gamma$  cuts through the Brillouin zone.  $\text{Im } \Sigma^{(2)}$ ,  $\text{Im } \Sigma^{(3)}$ , and the sum  $\text{Im } \Sigma^{(2)} + \text{Im } \Sigma^{(3)}$  are represented by dashed, dashed-dotted, and full lines, respectively.

Fig. 5. Imaginary parts of  $\Sigma_{\mathbf{k}}^{(2)}(\omega)$  and  $\Sigma_{\mathbf{k}}^{(3)}(\omega)$  at  $\Gamma$ ,  $X$ ,  $Z$ , and  $M$  points close to  $\omega = E_F$ .  $\text{Im } \Sigma^{(2)}$ ,  $\text{Im } \Sigma^{(3)}$ , and the sum  $\text{Im } \Sigma^{(2)} + \text{Im } \Sigma^{(3)}$  are represented by dashed, dashed-dotted, and full lines, respectively.

Fig. 6. Single-particle spectral function  $A_{\mathbf{k}}(\omega)$  along the  $\Gamma \rightarrow X$ ,  $X \rightarrow Z$ , and  $Z \rightarrow \Gamma$  cuts through the Brillouin zone.

Fig. 7. Quasiparticle dispersion (circles) derived from the maxima of the spectral function  $A_{\mathbf{k}}(\omega)$  and the unrenormalized dispersion (full line).

Fig. 8. Renormalized (full line) and unrenormalized (dashed line) density of states.

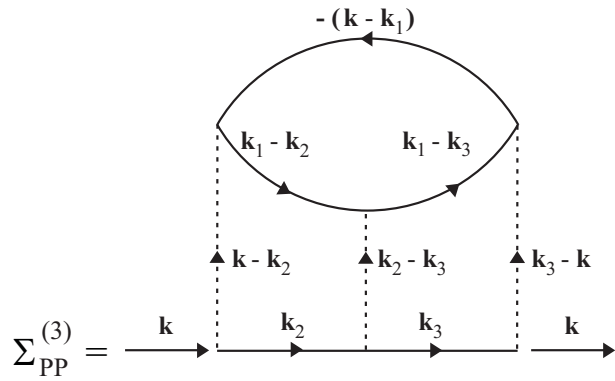
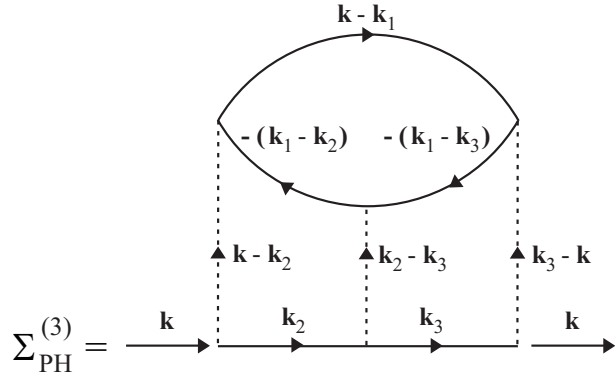
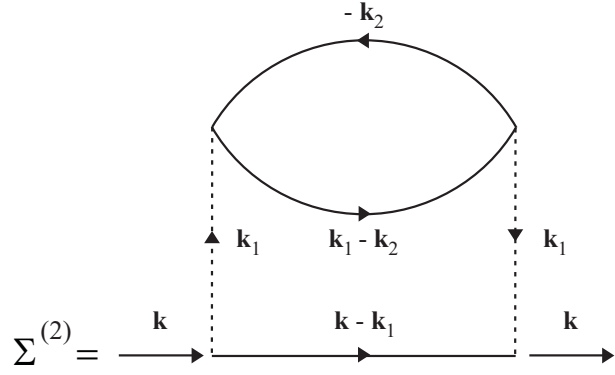


Figure 1: Diagrammatic representation of second- and third-order self-energy contributions.

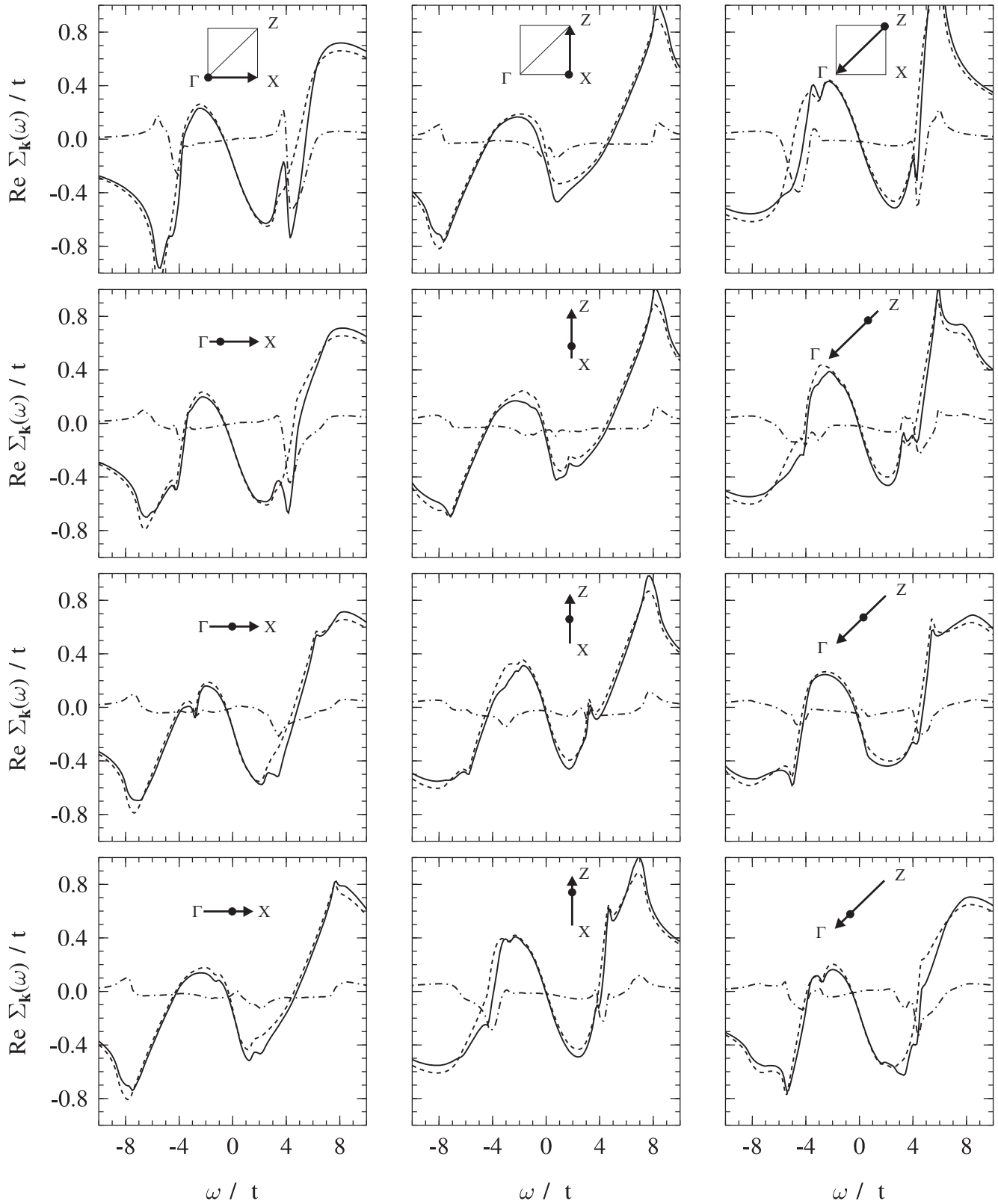


Figure 2: Real part of  $\Sigma_{\mathbf{k}}^{(3)}(\omega)$  along the  $\Gamma \rightarrow X$ ,  $X \rightarrow Z$ , and  $Z \rightarrow \Gamma$  cuts through the Brillouin zone.  $\text{Re} \Sigma_{\text{PH}}^{(3)}$ ,  $-\text{Re} \Sigma_{\text{PP}}^{(3)}$ , and  $\text{Re} \Sigma^{(3)} = \text{Re} \Sigma_{\text{PH}}^{(3)} + \text{Re} \Sigma_{\text{PP}}^{(3)}$  are represented by dashed, dashed-dotted, and full lines, respectively.

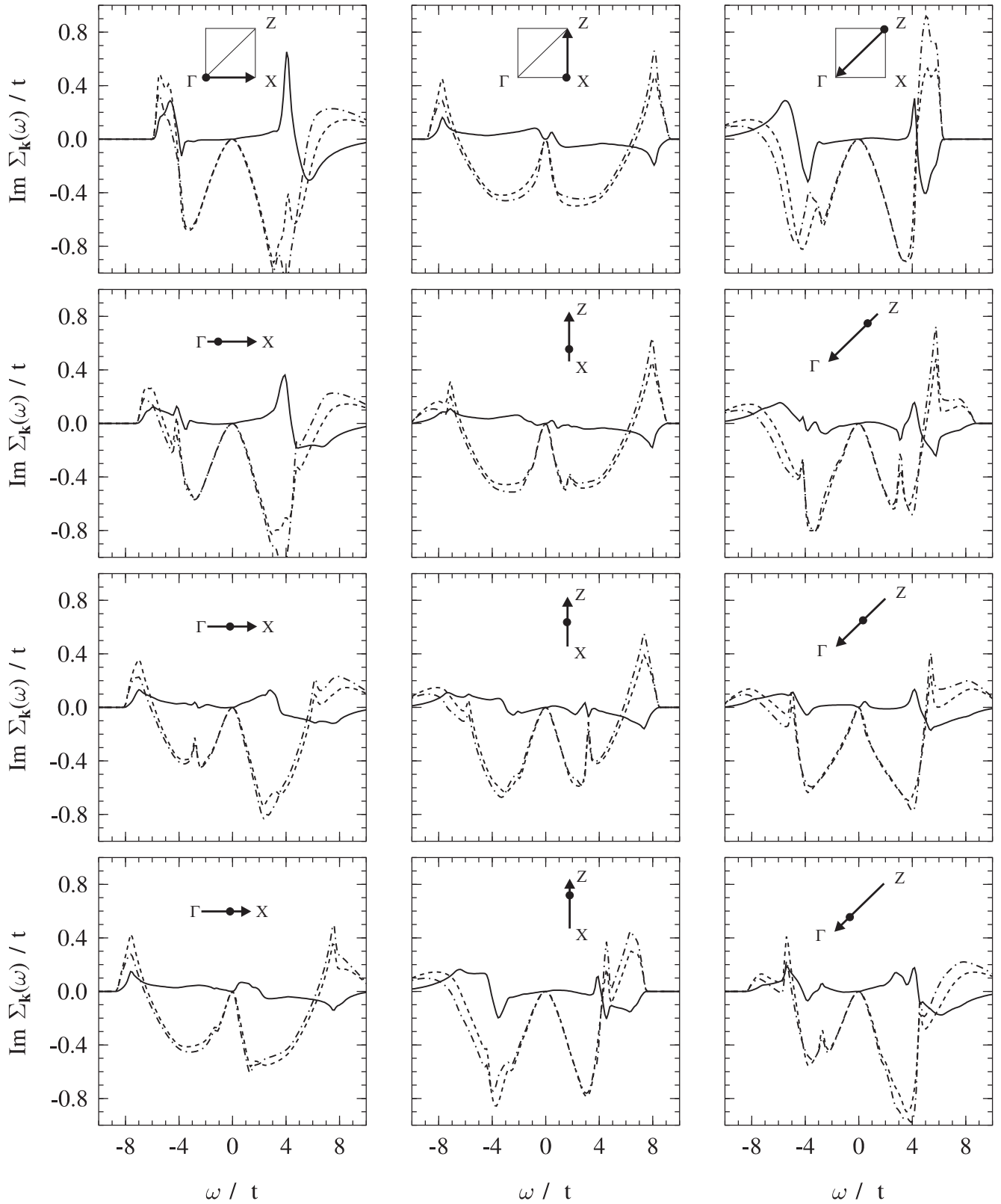


Figure 3: Imaginary part of  $\Sigma_{\mathbf{k}}^{(3)}(\omega)$  along the  $\Gamma \rightarrow X$ ,  $X \rightarrow Z$ , and  $Z \rightarrow \Gamma$  cuts through the Brillouin zone.  $\text{Im} \Sigma_{\text{PH}}^{(3)}$ ,  $-\text{Im} \Sigma_{\text{PP}}^{(3)}$ , and  $\text{Im} \Sigma^{(3)} = \text{Im} \Sigma_{\text{PH}}^{(3)} + \text{Im} \Sigma_{\text{PP}}^{(3)}$  are represented by dashed, dashed-dotted, and full lines, respectively.

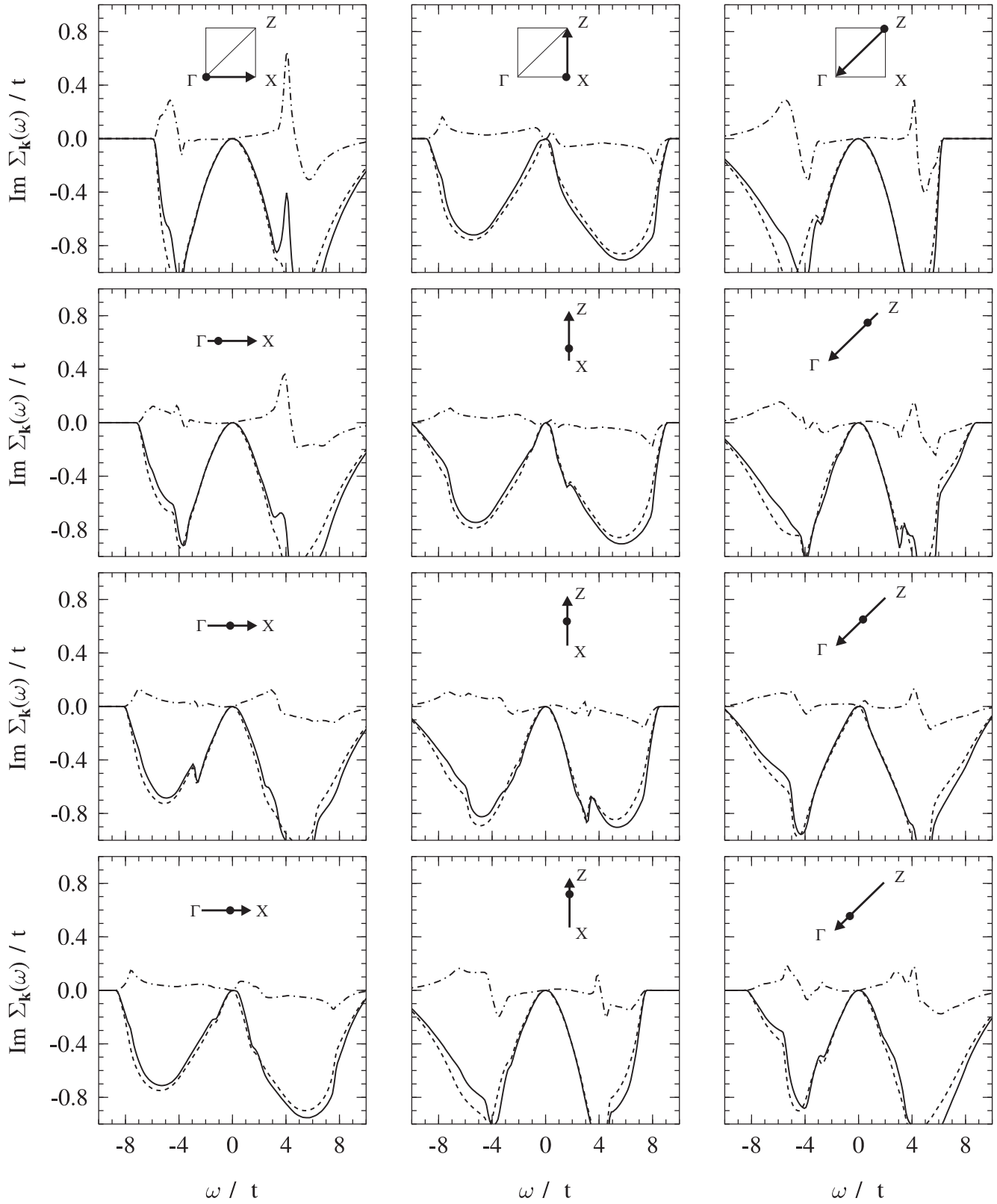


Figure 4: Imaginary parts of  $\Sigma_{\mathbf{k}}^{(2)}(\omega)$  and  $\Sigma_{\mathbf{k}}^{(3)}(\omega)$  along the  $\Gamma \rightarrow X$ ,  $X \rightarrow Z$ , and  $Z \rightarrow \Gamma$  cuts through the Brillouin zone.  $\text{Im} \Sigma^{(2)}$ ,  $\text{Im} \Sigma^{(3)}$ , and the sum  $\text{Im} \Sigma^{(2)} + \text{Im} \Sigma^{(3)}$  are represented by dashed, dashed-dotted, and full lines, respectively.

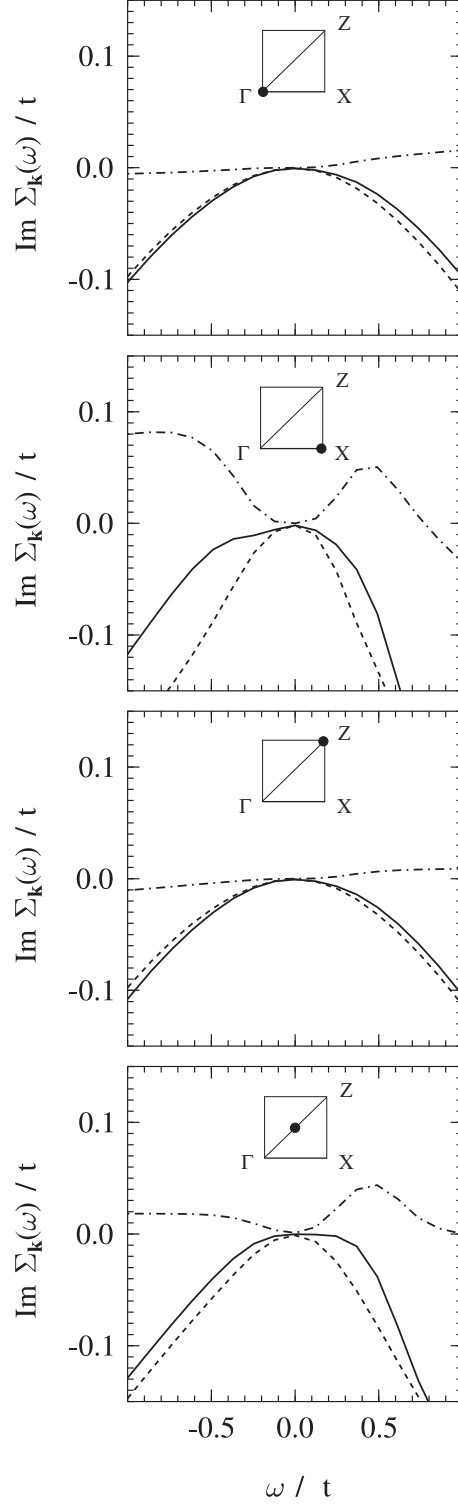


Figure 5: Imaginary parts of  $\Sigma_{\mathbf{k}}^{(2)}(\omega)$  and  $\Sigma_{\mathbf{k}}^{(3)}(\omega)$  at  $\Gamma$ , X, Z, and M points close to  $\omega = E_F$ .  $\text{Im} \Sigma^{(2)}$ ,  $\text{Im} \Sigma^{(3)}$ , and the sum  $\text{Im} \Sigma^{(2)} + \text{Im} \Sigma^{(3)}$  are represented by dashed, dashed-dotted, and full lines, respectively.

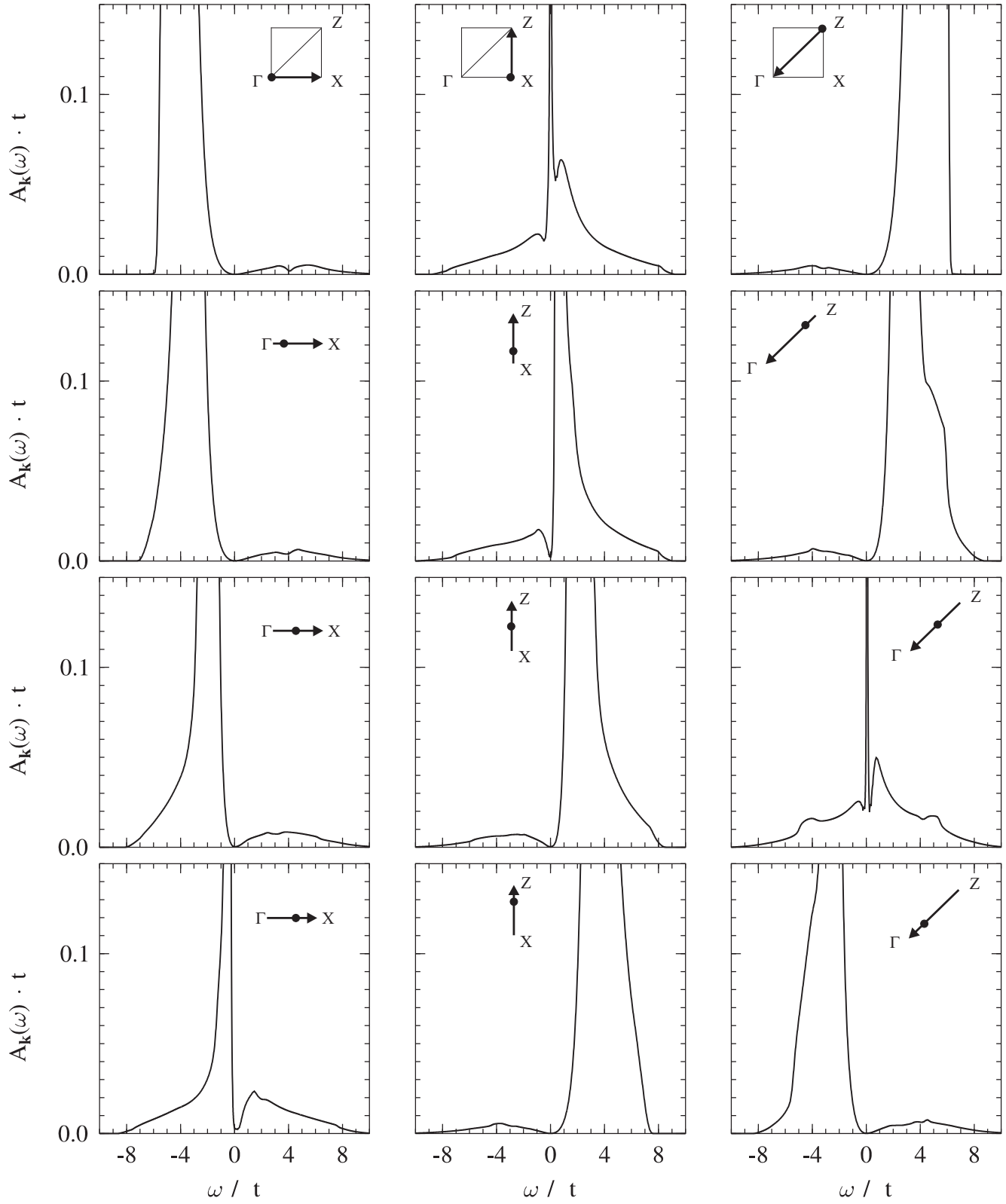


Figure 6: Single-particle spectral function  $A_{\mathbf{k}}(\omega)$  along the  $\Gamma \rightarrow X$ ,  $X \rightarrow Z$ , and  $Z \rightarrow \Gamma$  cuts through the Brillouin zone.

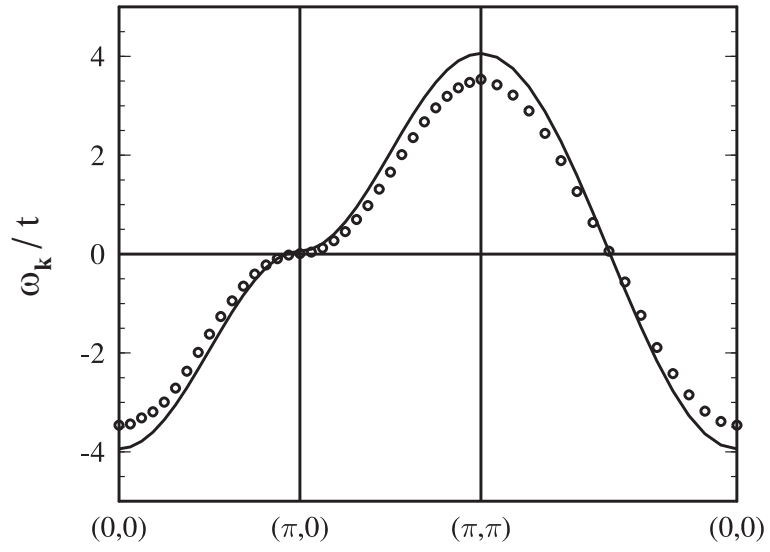


Figure 7: Quasiparticle dispersion (circles) derived from the maxima of the spectral function  $A_{\mathbf{k}}(\omega)$  and the unrenormalized dispersion (full line).

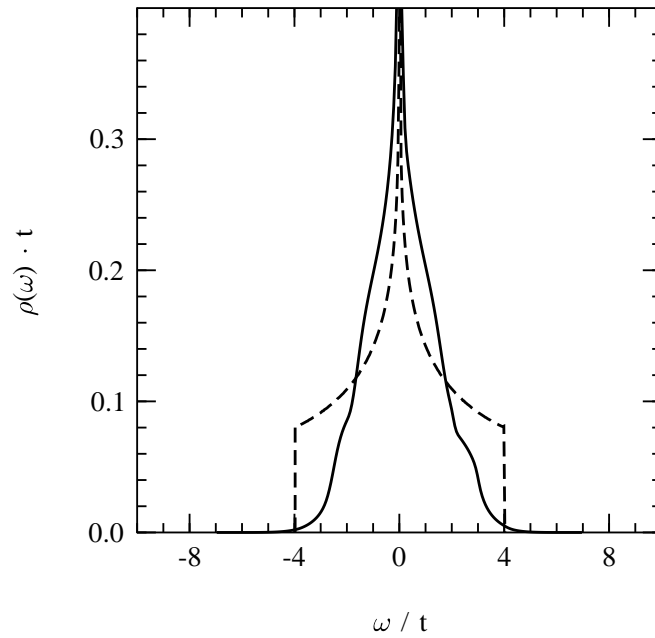


Figure 8: Renormalized (full line) and unrenormalized (dashed line) density of states.